Scattering of Magnons at Graphene Quantum-Hall-Magnet Junctions

Nemin Wei⬤, Chunli Huang, and Allan H. MacDonald

Department of Physics, The University of Texas at Austin, Austin, Texas 78712, USA

Motivated by recent nonlocal transport studies of quantum-Hall-magnet (QHM) states formed in monolayer graphene's $N = 0$ Landau level, we study the scattering of QHM magnons by gate-controlled junctions between states with different integer filling factors ν. For the $\nu = 1|-1|1$ geometry we find that magnons are weakly scattered by electric potential variation in the junction region, and that the scattering is chiral when the junction lacks a mirror symmetry. For the $\nu = 1|0|1$ geometry, we find that kinematic constraints completely block magnon transmission if the incident angle exceeds a critical value. Our results explain the suppressed nonlocal–voltage signals observed in the $\nu = 1|0|1$ case. We use our theory to propose that valley waves generated at $\nu = -1|1$ junctions and magnons can be used in combination to probe the spin or valley flavor structure of QHM states at integer and fractional filling factors.

Introduction.—The recent discovery of magnetic order in two-dimensional materials [1–5] has suggested new strategies to build ultracompact spintronic devices that utilize magnons as weakly dissipative information carriers [6–8]. Ordered states, referred to generically as quantum Hall magnets (QHMs), occur in graphene in a strong magnetic field and break spin and valley symmetries [9–25]. Because of their electronic simplicity and gate tunability, and also because the technology needed to prepare extremely clean and well characterized monolayer graphene samples is well established [26–29], graphene QHMs are an excellent system in which to demonstrate two-dimensional spintronic and magnonic device concepts.

When a strong magnetic field is applied perpendicular to a 2D graphene sheet, the π orbitals of the carbon atoms form Landau levels with approximate fourfold isospin degeneracy. The isospin degeneracy combines a twofold valley pseudospin with the electron spin degree of freedom. In a partially filled Landau level, Coulomb interactions often break the Hamiltonian's SU(4) isospin symmetry and give rise to a rich family of correlated insulating states. At an integer filling factor, the ground state is a single Slater determinant and can be therefore described by Hartree-Fock mean-field theory [24,30,31]. At filling factor $\nu = \pm 1$, i.e., at three-quarter and one-quarter filling of the $N = 0$ Landau level quartet, the ground state is analogous to the QHM states found in two-dimensional electron gases in semiconductor quantum wells and consists of fully spin and valley polarized electrons ($\nu = -1$) or holes ($\nu = 1$) [32]. In contrast, the ground state at filling factor $\nu = 0$ (half filling of the $N = 0$ Landau level) is more complicated. As pointed out by Kharitonov [24], the $\nu = 0$ phase diagram contains a ferromagnet (F), a canted antiferromagnet (CAF), a Kekulé distortion state, and a charge density wave. The competition between these states is

influenced by weak lattice-scale Coulomb interactions that break SU(4) symmetry, sample-dependent substrate-induced sublattice polarization potentials [33–35], dielectric screening [36], and in-plane magnetic fields. The systematic [13] dependence on in-plane magnetic field of an edge-state metal-insulator transition strongly suggests that the $\nu = 0$ ground state is a CAF in which opposite valleys have different spin polarizations. The ordered states at $\nu = 0$, ± 1 support low-energy collective excitations [16–18] that are analogous to magnon modes in conventional magnetic systems, and which we will refer to as QH magnons.

Recent experiments [37–41] have studied the transmission of QH magnons through junctions between distinct QHM states. In Refs. [38–41], $\nu = 1$ QH magnons are generated electrically by driving magnon-mediated transitions between conducting edge states with different spin orientations. The change in conduction spin is transferred to a magnon that can be propagated through the two-dimensional bulk. (See Ref. [42] for a theoretical model of the magnon generation process.) Magnons are then guided toward $1|\nu_m|1$ QHM junctions, where ν_m is a (gate-tunable) filling fraction of interest sandwiched between $\nu = 1$ regions. Any magnons transmitted through the junction generate nonlocal electrical signals on the opposite side of the device via the reciprocal of the magnon generation process. Measured nonlocal voltages suggest that the $1|-1|1$ junction is nearly transparent for magnons, since the nonlocal voltage signal is not greatly reduced by its presence. In contrast, the nonlocal voltage signal is greatly suppressed by $\nu = 1|0|1$ junctions. This finding requires an explanation since the $\nu_m = 0$ canted antiferromagnet also supports magnons [43–46].

In this Letter, we use microscopic theory to calculate magnon transmission through $1|\nu_m|1$ QHM junctions. For

$\nu_m = -1$ we find that although the magnon modes are identical in all regions, the electrostatic inhomogeneity of the junction partially reflects magnons. The $\nu_m = 0$ CAF state has two magnon branches that, except at very small momenta, have higher energies than $\nu = 1$ magnons. We find that this energy mismatch leads to perfect reflection above a critical angle of incidence Θ_c, explaining the difference in nonlocal electrical signals.

Generalized random phase approximation.—We formulate the problem of collective-mode transmission by studying the dynamics of the $N = 0$ Landau level single-particle density matrix

$$i\partial_t \hat{P}(t) = [\hat{H}, \hat{P}(t)], \tag{1}$$

where $\hat{H}$ is the mean-field Hamiltonian determined self-consistently at each instant in time:

$$\hat{H}_{k+q_y,k} = \hat{H}_k^0 \delta_{q_y,0} + \hat{\Sigma}_{k+q_y,k}^H + \hat{\Sigma}_{k+q_y,k}^F, \tag{2a}$$

$$\hat{H}_k^0 = -\frac{\Delta_z}{2}s^z - \frac{\Delta_v}{2}\tau^z + E_b(k), \tag{2b}$$

$$\hat{\Sigma}_{k+q_y,k}^H = \sum_{\alpha=0}^{z}\sum_{k'} V_\alpha(k-k', q_y)\mathrm{tr}(\tau^\alpha \hat{P}_{k'+q_y,k'})\tau^\alpha, \tag{2c}$$

$$\hat{\Sigma}_{k+q_y,k}^F = -\sum_{\alpha=0}^{z}\sum_{k'} V_\alpha(q_y, k-k')\tau^\alpha \hat{P}_{k'+q_y,k'}\tau^\alpha. \tag{2d}$$

The single-particle Hamiltonian $\hat{H}_k^0$, specified in Eq. (2b), includes Zeeman energy ($\Delta_z = \mathfrak{g}\mu_B|B|$), valley polarization energy (Δ_v) and background electrostatic (E_b) energy contributions. Δ_v is induced by adjacent hexagonal Boron-Nitride (hBN) layers if aligned and E_b controls the spatial variation of filling fraction. Here s (τ) are Pauli matrices in spin (valley) space and the wave vectors k are Landau gauge momenta in the direction along the junction line. The electrostatic background potential E_b is k dependent because Landau gauge eigenstates are localized along guiding center lines with x coordinate $X = kl_B^2$, where l_B is the magnetic length. In Eqs. (2c)–(2d), the $\alpha = 0$ and $\alpha = x, y, z$ self-energy terms account respectively for the SU(4) invariant long-range Coulomb interaction and the short-range valley-dependent interactions [47]. The time-independent self-consistent solutions of Eq. (1) preserve translational symmetry along the junction line and are therefore diagonal in k [48]:

$$\hat{P}_{k+q_y,k}^0 = \delta_{q_y,0}\sum_{m=0}^{3} f_{m,k}|k,m\rangle\langle k,m|, \tag{3}$$

where $|k,m\rangle$ is the mth mean-field band ordered energetically from 0 to 3 and $f_{m,k}$ is its occupation number. We plot the quasiparticle band structure of a $\nu = 1|-1|1$ junction
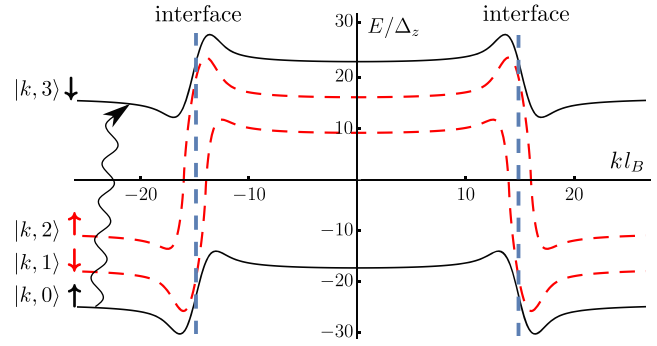

FIG. 1. Self-consistent Hartree-Fock band structure of a $1|-1|1$ junction in which the sense of valley polarization is opposite in the $\nu = 1$ and $\nu = -1$ regions. The uniform $\nu = 1$ and $\nu = -1$ states have majority ($\uparrow$) spin occupation selected by the weak Zeeman coupling and, for unaligned hBN encapsulation, spontaneously chosen valley polarization. The black solid lines show K valley quasiparticle energies vs guiding center, and the red dashed lines show the K' valley orbitals that cross the Fermi level ($E_F = 0$) at $\nu = 1|-1$ junctions. The curly line represents the bands involve in particle-hole transition of a $\nu = \pm 1$ magnon.

in Fig. 1 for future reference. To describe small amplitude dynamics, we expand $\hat{P}(t) = \hat{P}^0 + \delta\hat{P}(t)$ and use the compact notation

$$\psi_{kmn}(q_y, \omega) \equiv \int_{-\infty}^{\infty} dt\langle k+q_y, m|\delta\hat{P}(t)|k,n\rangle e^{i\omega t}, \tag{4}$$

to denote particle-hole transition amplitudes with momentum q_y. When linearized in $\delta\hat{P}$, Eq. (1) implies that

$$\omega\psi_{kmn}(q_y, \omega) = \sum_{k'm'n'} \mathbb{K}_{kmn}^{k'm'n'}(q_y)\psi_{k'm'n'}(q_y, \omega), \tag{5}$$

where ω is the collective mode frequency and $\mathbb{K}_{kmn}^{k'm'n'}$ is the RPA kernel that acts as a superoperator on the collective mode ψ [47]. Equation (5) is known as the generalized RPA equation [49–51].

Magnon scattering.—The magnon scattering problem is complicated by the strong nonlocality of the RPA kernel $\mathbb{K}_{kmn}^{k'm'n'}(q_y)$. In the absence of a junction $\mathbb{K}_{kmn}^{k'm'n'}(q_y)$ is invariant under simultaneous translation of guiding centers kl_B^2 and $k'l_B^2$, allowing Eq. (5) to be solved by Fourier transformation to obtain bulk modes labeled by two-dimensional wave vectors $\mathbf{q} = (q_x, q_y)$ with energies $\omega_i(\mathbf{q})$. Some key properties of the bulk collective modes are briefly summarized in Table I. Since q_y remains a good quantum number in the presence of a $1|\nu_m|1$ junction, we are left with a q_y-dependent one-dimensional scattering problem with the $\nu = 1$ bulk modes as asymptoptic states. We therefore apply the scattering boundary conditions

TABLE I. Properties of the magnon mode ω_s of the $\nu = 1$ F state and the two magnon modes $\omega_{1,2}$ of the $\nu = 0$ CAF state. The CAF modes are linear-combinations of spin-flips in the K and K' valleys (A and B sublattices) [47].

ν	Modes	Gap	Description
± 1	ω_s	Δ_z	Spin precession in a single valley
0	ω_1	0	In-plane($\perp B$) oscillation of Néel vector $\mathbf{n}$
0	ω_2	Δ_z	Precession of spin-polarization $\mathbf{m}$ about B field

$$\psi_{k30}(q_y, \omega) = \begin{cases} e^{iq_x k l_B^2} + r(q_y, \omega) e^{-iq_x k l_B^2}, & k \to -\infty \\ t(q_y, \omega) e^{iq_x k l_B^2}, & k \to \infty \end{cases}$$

$$\psi_{kmn}(q_y, \omega) = 0, \qquad k \to \pm\infty \quad \text{and} \quad m, n \neq (3, 0).$$
(6)

The asymptotic states are pure (ψ_{k30}) $\nu = 1$ magnons that are gapped by the Zeeman energy [38,39]. In Eq. (6) q_x is determined by solving $\omega_s(\mathbf{q}) = \omega$, see Table I. We solve for the scattering states and the q_y-dependent reflection $r(q_y, \omega)$ and transmission $t(q_y, \omega)$ coefficients by discretizing k, applying Eq. (5) at $j = 1, \ldots, N$ points in a scattering region centered on the junction, and substituting the asymptotic expressions for $\psi_{k'm'n'}(q_y, \omega)$ at $j = 1$, $j = N$, and outside the junction. Only the $m, n = (3, 0)$ RPA equation is applied at $j = 1$ and $j = N$, which are

assumed to be in the asymptotic region. This procedure yields a set of inhomogeneous linear equations [47] that we have converged with respect to guiding center mesh density to obtain the results discussed below.

Magnon transmission results.—Our results for the magnon transmission probabilities $T(q_y, \omega) = |t(q_y, \omega)|^2$ of $1|\nu_m|1$ QHM junctions with $\nu_m = -1$ and $\nu_m = 0$ are shown in Figs. 2(a) and 2(d), respectively. Both junctions have a threshold energy ω_{tr}, below which there is no transmission, $T(q_y, \omega < \omega_{tr}) = 0$. For a $1|-1|1$ junction, the bulk $\nu = \pm 1$ regions have identical magnon dispersions, so the threshold energy is simply the bulk magnon energy at normal incidence: $\omega_{tr} = \omega_s(0, q_y)$. For $\omega > \omega_{tr}$, we find magnon transmission decreases with increasing q_y. The reduction is due to a peculiar property of collective mode excitations in quantum Hall systems, namely, that the center-of-mass momentum $\mathbf{q}$ of a particle-hole excitation is related to its electric-dipole moment $\mathbf{p}$ by [52–54], $\mathbf{p} = |e| l_B^2 \hat{z} \times \mathbf{q}$, as illustrated in Fig. 2(c). Magnons with larger q_y scatter more strongly off the electric fields $E\hat{x}$ present in the junction region. When we examine the $1|-1$ and $-1|1$ junctions separately, we find that magnons with opposite signs of q_y have different transmission probabilities, as shown in Fig. 2(b). This behavior is expected since the $1|-1$ junction acts like a repulsive scatterer when the dipole moment has an $\hat{x}$ projection opposite to the junction electric field, and like an attractive scatterer when the $\hat{x}$ projection has a dipole moment that is aligned with
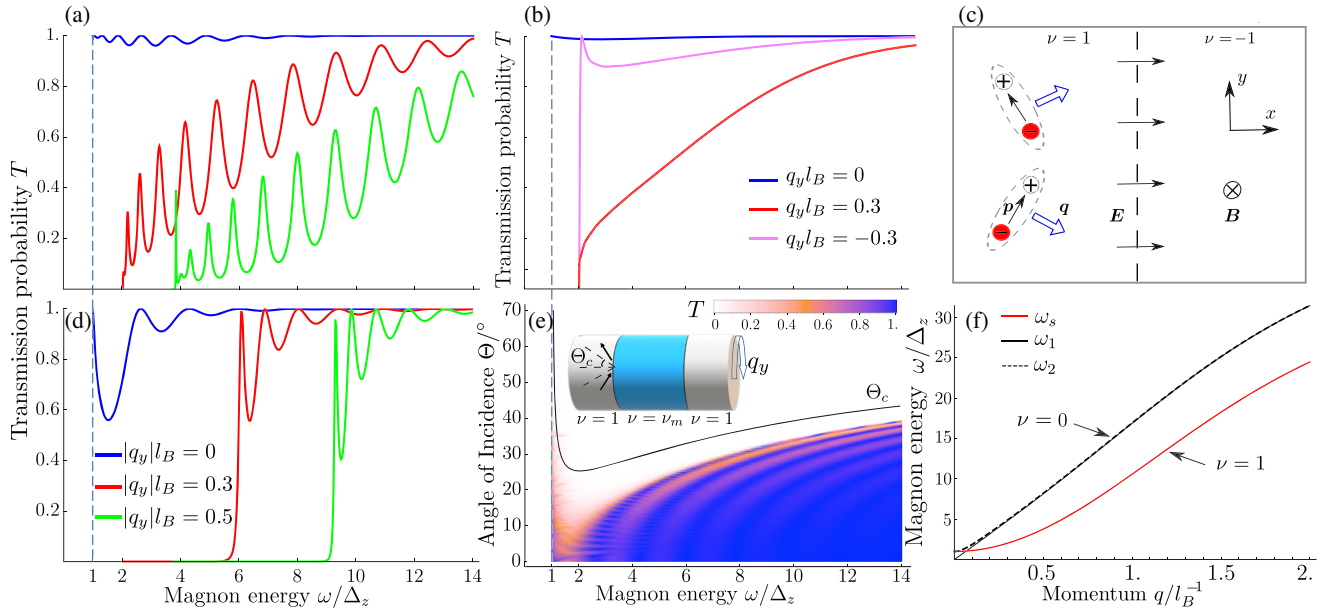

FIG. 2. Magnon transmission probabilities $T(q_y, \omega)$ vs ω for $\nu = 1|-1|1$ (a), $\nu = 1|-1$ (b) and $\nu = 1|0|1$ (d) QHM junctions [47]. (c) Schematic particle-hole pairs in $\nu = 1|-1$ junctions. The interfacial electric field $\mathbf{E}$ points from $\nu = 1$ to $\nu = -1$. Negative (positive) signs represents electrons (holes). The dipole moment $\mathbf{p}$ of electron-hole pairs is perpendicular to both the magnetic field $\mathbf{B}$ and the center-of-mass momentum $\mathbf{q}$. (e) Color plot of the magnon transmission probability through a $\nu = 1|0|1$ junction vs energy and angle of incidence. (f) Magnon dispersions in uniform $\nu = \pm 1$ F states (ω_s) and in $\nu = 0$ ($\omega_{1,2}$) CAF states. These results are generated with experimental determined Coulomb interaction strength at $B = 8$ T [47] in a geometry with width $L_y = 80\pi l_B$ and the length of ν_m region is $30 l_B$.

the junction electric field. The total transmission through the $1|-1|1$ junction plotted in Figs. 2(a) and 2(d) has $q_y \to -q_y$ symmetry because the studied model has mirror symmetry about the $y-z$ plane at the center of the $\nu = \nu_m$ region. We have verified that the junction scattering becomes chiral when this symmetry is absent.

The threshold energy ω_{tr} in Fig. 2(d) ($1|0|1$ junction) appears to be significantly larger than in Fig. 2(a) ($1|-1|1$ junction). The suppressed magnon transmission is due to a mismatch between CAF and F collective mode dispersions. As shown in Fig. 2(f), the bulk collective modes of $\nu = 0$ CAFs disperse more strongly than those of $\nu = 1$ Fs, so that $\omega_{1,2}$ has higher energy than ω_s, except at very small momenta where ω_1 is gapless while ω_2 and ω_s are gapped. To transmit a $\nu = 1$ magnon with energy $\omega = \omega_s$ and parallel momentum q_y through $1|0$ junction, the conservation of energy and parallel momentum requires that

$$\omega_s(q_x^L, q_y) = \omega_1(q_x^R, q_y), \tag{7}$$

where $q_x^{L/R} \geq 0$ are the asymptotic normal momenta on the left (L) and right (R) sides of the $1|0$ junction. We identify the threshold energy as $\omega_1(0, q_y)$, the value of ω for which $q_x^R \to 0$. Since $\omega_1(0, q_y) > \omega_s(0, q_y)$ we conclude that the $1|0|1$ junction has a higher threshold energy than $1|-1|1$ junction. Once the incoming magnon energy exceeds $\omega_{tr}(q_y)$, as illustrated in Fig. 2(d), T rapidly approaches 1. This property can be understood by noting the valley polarization of superpositions of ω_1 and ω_2 modes vary on the long length scale $\lambda_0 = (q_{x1}^R - q_{x2}^R)^{-1}$, where q_{x1}^R and q_{x2}^R are the nearly identical local x wave vectors of the nearly degenerate [Fig. 2(f)] $\omega_{1,2}$ modes. A $\nu = 0$ magnon can therefore maintain the valley polarization of the $\nu = 1$ magnon across the junction, provided that the ν_m region is shorter than λ_0. Our results for $1|0|1$ junction magnon transmission are summarized in Fig. 2(e), in which the transmission probability is plotted as a function of energy and angle of incidence $\Theta = \arctan(q_y/q_x^L)$. The black curve shows the critical incident angle Θ_c, obtained by solving Eq. (7) with $q_x^R = 0$. For higher angles of

incidence, momentum and energy conservation imply that the magnons are evanescent waves in the $\nu = 0$ region.

The transmission probabilities in Fig. 2 exhibit Fabry-Pérot oscillations generated by the repeated scattering at the two interfaces. The interference pattern will be smeared out in observables when the experimental device [38] allows a magnon to incident on the magnetic junction from all angles. It is therefore more informative to calculate the average magnon transmission probability:

$$\bar{T}(\omega) \equiv \frac{1}{\pi} \int_{-\pi/2}^{\pi/2} d\theta \, T(q_y(\theta, \omega), \omega). \tag{8}$$

As shown in Fig. 3(a), the average transmission $\bar{T}$ through a $1|0|1$ junction is noticeably smaller than the transmission through a $1|-1|1$ junction at low energies but becomes comparable to a $1|-1|1$ junction at high energy. In our calculation of $1|0|1$ junction we assumed perfect screening of induced Hartree potentials in the junction region by nearby gates [48]. Since the inhomogeneity of the electrostatic potential is a source of magnon reflection, the transmission through a $1|0|1$ junction would be even lower if we accounted for imperfect screening.

Discussion.—We now use our findings to interpret the experimental results in Ref. [38] and to propose related studies that might be informative. Magnons can be generated electrically by bringing edge channels with opposite spins and different chemical potentials together at a hot spot, opening a path for magnon-generation mediated edge-channel spin flips. The energies of magnons generated in this way are smaller than the electrical bias voltage. Magnons will radiate out from the hotspot and those transmitted through the interface will generate a nonlocal voltage via the reciprocal of the injection process.

For a $1|0|1$ junction, the measured nonlocal voltage [38] is small even when the electrical bias voltage is raised to $\sim 5\Delta_z$. Our calculations show that this behavior is explained by the larger energies of magnons in $\nu = 0$ regions compared to $\nu = 1$ regions and the associated threshold energy for magnon transmission in Fig. 2(d). The slow
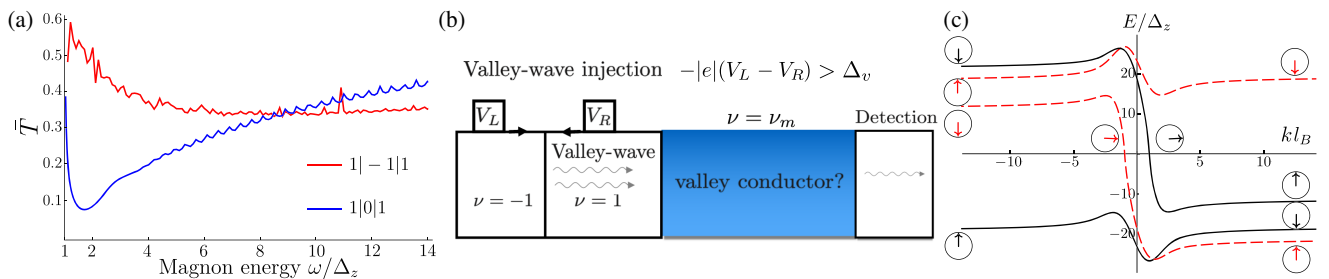

FIG. 3. (a) Angularly average magnon transmission $\bar{T}(\omega)$ vs ω. The parameters used in this calculation are the same as those in Fig. 2. (b) Valley wave scattering devices. We propose to replace the $2|1$ junction used in Refs. [38,39] with $-1|1$ junctions to generate valley waves. (c) Band structure of a $-1|1$ junction used for valley-wave injection. All states color-coded with black and red are, respectively, fully polarized in K and K' valleys, while the spin rotates smoothly from ↑ to ↓ across the junction. For this calculation, valley polarization energy $\Delta_v = 3.7$ meV correspond to the circumstances of Ref. [39].

increase in average transmission probability $\bar{T}$ with magnon energy we find is also in agreement with experimental trends[38]. We do find a peak in $\bar{T}$ [cf. Fig. 3(a)] in a narrow window of energy ($1 < \omega/\Delta_z < 1.2$) just above Δ_z where the $\nu = 0$ and $\nu = 1$ magnon energies are more similar that is not detected experimentally, presumably because magnon generation in this energy window is not sufficient to produce an observable signal.

The experimental nonlocal signals of $1|1|1$ and $1|-1|1$ junctions are similar for bias voltages $\lesssim 5\Delta_z$, and much larger than the voltages measured in the $1|0|1$ case. In our theory this property is due to the fact that $\nu = 1$ and $\nu = -1$ magnon modes have identical dispersions and therefore no kinematic transmission constraints. Our theory does predict finite reflection at $1|-1|1$ junctions that is absent in the translationally invariant $1|1|1$ case, but this will not be observable if unintended scattering from disorder or the split gate junctions dominates magnon scattering. Indeed, as we have emphasized, our calculation has identified the electrical dipole moments of QH magnons as a mechanism for magnon scattering off variations in electrical potential. Other extrinsic mechanisms such as spin-dependent disorder [55–57] near the sample edges can also suppress magnon transmission but are unlikely to play a dominant role in high quality devices used in Refs. [38,39].

Our theory emphasizes the general physical principle behind magnon transmission and its suppression in a $1|\nu|1$ magnetic junction. If the theory were applied to a specific *mesoscopic* device, the device geometry including locations of contacts would need to be taken into account to quantitatively interpret the nonlocal voltage. However, note that the transmission probability calculated on the cylinder is applicable to more complicated geometry as long as the interface is smooth in the magnetic length scale and the magnon momentum parallel to the interface is locally well defined.

In closing, we propose an experimental protocol illustrated schematically in Fig. 3(b) to electrically generate valley waves using the $\nu = -1|1$ junction. As shown in Fig. 3(c), when the $-1|1$ interface receives finite valley polarization potential from the aligned hBN, the mean-field band structure hosts two edge states with opposite valley polarization and nearly parallel spins whose chemical potentials can be independently controlled via the contacting geometry illustrated in Fig. 3(b). The bias voltage opens up a path for valley-wave generation scattering between edge channels. In order to increase valley-wave emission probability, the edge states can be brought into close proximity via a quantum point contact. We expect the emitted valley waves to be transmitted through ground states that support valley-wave excitations. Measuring nonlocal voltages provides a new method to determine the isospin structure of quantum Hall ground-states, which remains an elusive target especially at fractional filling factors [35]. In a broader context, the quantum-Hall-magnet

junctions [37–41] provide a simple operational way of thinking about the transport of spin fluctuations across the interfaces of different magnetic materials. This can help to understand and test new spintronic ideas and have potential applications to magnon-based logic devices [58].

[1] N. Samarth, Condensed-matter physics: Magnetism in flatland, Nature (London) **546,** 216 (2017).

[2] M. Gibertini, M. Koperski, A. Morpurgo, and K. Novoselov, Magnetic 2d materials and heterostructures, Nat. Nanotechnol. **14,** 408 (2019).

[3] K. S. Burch, D. Mandrus, and J.-G. Park, Magnetism in two-dimensional van der Waals materials, Nature (London) **563,** 47 (2018).

[4] B. Huang, G. Clark, D. R. Klein, D. MacNeill, E. Navarro-Moratalla, K. L. Seyler, N. Wilson, M. A. McGuire, D. H. Cobden, D. Xiao *et al.*, Electrical control of 2d magnetism in bilayer cri 3, Nat. Nanotechnol. **13,** 544 (2018).

[5] S. Jiang, L. Li, Z. Wang, K. F. Mak, and J. Shan, Controlling magnetism in 2d cri 3 by electrostatic doping, Nat. Nanotechnol. **13,** 549 (2018).

[6] A. Chumak, V. Vasyuchka, A. Serga, and B. Hillebrands, Magnon spintronics, Nat. Phys. **11,** 453 (2015).

[7] A. V. Chumak, Fundamentals of magnon-based computing, arXiv:1901.08934.

[8] S. M. Rezende, Magnon spintronics, in *Fundamentals of Magnonics* (Springer, New York, 2020), pp. 287–352.

[9] Y. Zhang, Z. Jiang, J. P. Small, M. S. Purewal, Y.-W. Tan, M. Fazlollahi, J. D. Chudow, J. A. Jaszczak, H. L. Stormer, and P. Kim, Landau-Level Splitting in Graphene in High Magnetic Fields, Phys. Rev. Lett. **96,** 136806 (2006).

[10] J. G. Checkelsky, L. Li, and N. P. Ong, Zero-Energy State in Graphene in a High Magnetic Field, Phys. Rev. Lett. **100,** 206801 (2008).

[11] X. Du, I. Skachko, F. Duerr, A. Luican, and E. Y. Andrei, Fractional quantum Hall effect and insulating phase of dirac electrons in graphene, Nature (London) **462,** 192 (2009).

[12] A. F. Young, C. R. Dean, L. Wang, H. Ren, P. Cadden-Zimansky, K. Watanabe, T. Taniguchi, J. Hone, K. L. Shepard, and P. Kim, Spin and valley quantum Hall ferromagnetism in graphene, Nat. Phys. **8,** 550 (2012).

[13] A. Young, J. Sanchez-Yamagishi, B. Hunt, S. Choi, K. Watanabe, T. Taniguchi, R. Ashoori, and P. Jarillo-Herrero, Tunable symmetry breaking and helical edge transport in a graphene quantum spin Hall state, Nature (London) **505,** 528 (2014).

[14] M. O. Goerbig, Electronic properties of graphene in a strong magnetic field, Rev. Mod. Phys. **83,** 1193 (2011).

[15] M. O. Goerbig, R. Moessner, and B. Douçot, Electron interactions in graphene in a strong magnetic field, Phys. Rev. B **74,** 161407(R) (2006).

[16] J. Alicea and M. P. A. Fisher, Graphene integer quantum Hall effect in the ferromagnetic and paramagnetic regimes, Phys. Rev. B **74,** 075422 (2006).

[17] K. Yang, S. Das Sarma, and A. H. MacDonald, Collective modes and Skyrmion excitations in graphene $su(4)$ quantum Hall ferromagnets, Phys. Rev. B **74,** 075423 (2006).

[18] R. L. Doretto and C. M. Smith, Quantum Hall ferromagnetism in graphene: Su(4) bosonization approach, Phys. Rev. B **76,** 195431 (2007).

[19] I. F. Herbut, Theory of integer quantum Hall effect in graphene, Phys. Rev. B **75,** 165411 (2007).

[20] J. Jung and A. H. MacDonald, Theory of the magnetic-field-induced insulator in neutral graphene sheets, Phys. Rev. B **80,** 235417 (2009).

[21] K. Nomura, S. Ryu, and D.-H. Lee, Field-Induced Kosterlitz-Thouless Transition in the $n = 0$ Landau Level of Graphene, Phys. Rev. Lett. **103,** 216801 (2009).

[22] R. Nandkishore and L. Levitov, Spontaneously ordered states in bilayer graphene, Phys. Scr. **T146,** 014011 (2012).

[23] M. Kharitonov, Canted Antiferromagnetic Phase of the $\nu = 0$ Quantum Hall State in Bilayer Graphene, Phys. Rev. Lett. **109,** 046803 (2012).

[24] M. Kharitonov, Phase diagram for the $\nu = 0$ quantum Hall state in monolayer graphene, Phys. Rev. B **85,** 155439 (2012).

[25] I. Sodemann and A. H. MacDonald, Broken Su(4) Symmetry and the Fractional Quantum Hall Effect in Graphene, Phys. Rev. Lett. **112,** 126804 (2014).

[26] C. Dean, P. Kim, J. Li, and A. Young, Fractional quantum Hall effects in graphene, in Fractional Quantum Hall Effects: New Developments (World Scientific, Singapore, 2020), Vol. **317.**

[27] C. R. Dean, A. F. Young, I. Meric, C. Lee, L. Wang, S. Sorgenfrei, K. Watanabe, T. Taniguchi, P. Kim, K. L. Shepard *et al.*, Boron nitride substrates for high-quality graphene electronics, Nat. Nanotechnol. **5,** 722 (2010).

[28] C. R. Dean, A. F. Young, P. Cadden-Zimansky, L. Wang, H. Ren, K. Watanabe, T. Taniguchi, P. Kim, J. Hone, and K. Shepard, Multicomponent fractional quantum Hall effect in graphene, Nat. Phys. **7,** 693 (2011).

[29] A. A. Zibrov, C. Kometter, H. Zhou, E. Spanton, T. Taniguchi, K. Watanabe, M. Zaletel, and A. Young, Tunable interacting composite fermion phases in a half-filled bilayer-graphene landau level, Nature (London) **549,** 360 (2017).

[30] S. M. Girvin, The quantum Hall effect: Novel excitations and broken symmetries, in *Aspects Topologiques de la Physique en Basse Dimension* Topological Aspects of Low Dimensional Systems (Springer, New York, 1999), pp. 53–175.

[31] K. Nomura and A. H. MacDonald, Quantum Hall Ferromagnetism in Graphene, Phys. Rev. Lett. **96,** 256602 (2006).

[32] D. A. Abanin, B. E. Feldman, A. Yacoby, and B. I. Halperin, Fractional and integer quantum Hall effects in the zeroth Landau level in graphene, Phys. Rev. B **88,** 115407 (2013).

[33] B. Hunt, J. Sanchez-Yamagishi, A. Young, M. Yankowitz, B. J. LeRoy, K. Watanabe, T. Taniguchi, P. Moon, M. Koshino, P. Jarillo-Herrero *et al.*, Massive Dirac fermions and Hofstadter butterfly in a van der Waals heterostructure, Science **340,** 1427 (2013).

[34] F. Amet, J. R. Williams, K. Watanabe, T. Taniguchi, and D. Goldhaber-Gordon, Insulating Behavior at the Neutrality Point in Single-Layer Graphene, Phys. Rev. Lett. **110,** 216601 (2013).

[35] A. Zibrov, E. Spanton, H. Zhou, C. Kometter, T. Taniguchi, K. Watanabe, and A. Young, Even-denominator fractional quantum Hall states at an isospin transition in monolayer graphene, Nat. Phys. **14,** 930 (2018).

[36] L. Veyrat, C. Déprez, A. Coissard, X. Li, F. Gay, K. Watanabe, T. Taniguchi, Z. Han, B. A. Piot, H. Sellier *et al.*, Helical quantum Hall phase in graphene on SrTiO3, Science **367,** 781 (2020).

[37] P. Stepanov, S. Che, D. Shcherbakov, J. Yang, R. Chen, K. Thilahar, G. Voigt, M. W. Bockrath, D. Smirnov, K. Watanabe *et al.*, Long-distance spin transport through a graphene quantum Hall antiferromagnet, Nat. Phys. **14,** 907 (2018).

[38] D. S. Wei, T. van der Sar, S. H. Lee, K. Watanabe, T. Taniguchi, B. I. Halperin, and A. Yacoby, Electrical generation and detection of spin waves in a quantum Hall ferromagnet, Science **362,** 229 (2018).

[39] H. Zhou, H. Polshyn, T. Taniguchi, K. Watanabe, and A. Young, Solids of quantum Hall skyrmions in graphene, Nat. Phys. **16,** 154 (2020).

[40] H. Zhou, C. Huang, N. Wei, T. Taniguchi, K. Watanabe, M. P. Zaletel, Z. Papić, A. H. MacDonald, and A. F. Young, Strong-magnetic-field magnon transport in monolayer graphene, arXiv:2102.01061.

[41] A. Assouline, M. Jo, P. Brasseur, K. Watanabe, T. Taniguchi, T. Jolicoeur, P. Roche, D. C. Glattli, N. Kumada, F. D. Parmentier, and P. Roulleau, Unveiling excitonic properties of magnons in a quantum Hall ferromagnet, arXiv:2102.02068.

[42] C. Huang, N. Wei, and A. MacDonald (to be published).

[43] G. Murthy, E. Shimshoni, and H. A. Fertig, Collective bulk and edge modes through the quantum phase transition in graphene at $\nu = 0$, Phys. Rev. B **93,** 045105 (2016).

[44] S. Takei, A. Yacoby, B. I. Halperin, and Y. Tserkovnyak, Spin Superfluidity in the $\nu = 0$ Quantum Hall State of Graphene, Phys. Rev. Lett. **116,** 216801 (2016).

[45] J. R. M. de Nova and I. Zapata, Symmetry characterization of the collective modes of the phase diagram of the $\nu = 0$ quantum Hall state in graphene: Mean-field phase diagram and spontaneously broken symmetries, Phys. Rev. B **95,** 165427 (2017).

[46] F. Pientka, J. Waissman, P. Kim, and B. I. Halperin, Thermal Transport Signatures of Broken-Symmetry Phases in Graphene, Phys. Rev. Lett. **119,** 027601 (2017).

[47] See Supplemental Material at http://link.aps.org/supplemental/10.1103/PhysRevLett.126.117203 for the details of the model, the properties of the collective modes, and the numeric methods to calculate transmission probability of collective modes.

[48] N. Wei, C. Huang, and A. MacDonald (to be published).

[49] D. Pines and P. Nozieres, Theory of quantum liquids: Normal fermi liquids, *Advanced Book Classics* (Westview Press, 1994).

[50] J. W. Negele, The mean-field theory of nuclear structure and dynamics, Rev. Mod. Phys. **54,** 913 (1982).

[51] P. Ring and P. Schuck, *The Nuclear Many-Body Problem* (Springer Science & Business Media, New York, 2004).

[52] L. Gor'kov and I. Dzyaloshinskii, Contribution to the theory of the Mott exciton in a strong magnetic field, Sov. Phys. JETP **26**, 449 (1968).

[53] C. Kallin and B. I. Halperin, Excitations from a filled Landau level in the two-dimensional electron gas, Phys. Rev. B **30**, 5655 (1984).

[54] J. Cao, H. A. Fertig, and L. Brey, Quantum geometric exciton drift velocity, arXiv:2008.00259.

[55] P. Tikhonov, E. Shimshoni, H. A. Fertig, and G. Murthy, Emergence of helical edge conduction in graphene at the $\nu = 0$ quantum Hall state, Phys. Rev. B **93**, 115137 (2016).

[56] J.-H. Zheng and M. A. Cazalilla, Nontrivial interplay of strong disorder and interactions in quantum spin-Hall insulators doped with dilute magnetic impurities, Phys. Rev. B **97**, 235402 (2018).

[57] C. Huang and M. A. Cazalilla, Disorder effects on helical edge transport in graphene under a strong tilted magnetic field, Phys. Rev. B **92**, 155124 (2015).

[58] B. Lenk, H. Ulrichs, F. Garbs, and M. Münzenberg, The building blocks of magnonics, Phys. Rep. **507**, 107 (2011).